RANS and Hybrid RANS-LES Results for the Fourth High-Lift Prediction Workshop using the NSU3D Solver

Mark C. Bogstad[1], Andrew C. Kirby[2], and Dimitri J. Mavriplis*[2]

[1] *Scientific Simulations LLC, Laramie, WY, USA*
[2] *University of Wyoming, Laramie, WY, USA*

Computational fluid dynamics results for the high-lift common research model test cases that were the subject of the fourth High Lift Prediction Workshop are described in this paper. Two different approaches are used in this work. In the first approach, fixed grid steady-state Reynolds-averaged Navier-Stokes (RANS) solutions were obtained on unstructured meshes using a traditional second-order accurate finite-volume solver using unstructured mixed element meshes. A second set of results was obtained using a hybrid RANS-LES approach using a dual-solver overset-mesh paradigm. In this approach the same RANS solver and meshes are used in the near body region, while in the off-body region a high-order discontinuous Galerkin discretization is used in conjunction with an adaptively refined Cartesian mesh, which is overlaid on the near-body mesh. The fixed grid RANS results include the following workshop defined test cases: a flap deflection study, a grid refinement study, and a $C_{L_{max}}$ study. The hybrid RANS-LES results were only run for the nominal flap configuration at two angles of attack due to resource limitations. In general, the fixed grid RANS results agree with the collective RANS results obtained from the workshop. $C_{L_{max}}$ is predicted reasonably well, although post-stall C_L values drop off much more significantly than observed experimentally and discrepancies between computed and experimental flow separation patterns are observed. The hybrid RANS-LES results show equivalent accuracy to the RANS results for the low angle of attack case (pre-stall) and show significant improvement in the post-stall region over the RANS results as compared to experimental data, although the magnitude of the pitching moment is still underpredicted. Although the hybrid RANS-LES approach shows promise for separated flow regimes, additional work is required to fully understand the effects of grid and time-step resolution, as well as adaptive mesh refinement criteria on overall accuracy and computational expense.

I. Introduction

This paper documents the results obtained for the fourth high-lift prediction workshop test cases using two different approaches, namely a steady-state Reynolds-averaged Navier-Stokes (RANS) methodology and a hybrid RANS-LES methodology. The fourth High-lift Prediction Workshop (HLPW4) was held concurrently with the third Geometry and Mesh Generation Workshop (GMGW3) in January 2022, alongside the AIAA Scitech Forum. HLPW4 and GMGW3 employed a different format than previous workshops, which was conceived with the goal of promoting and assessing the capabilities of new computational technologies for high-lift aerodynamic problems. The HLPW/GMGW workshops were organized around Technical Focus Groups (TFG) which covered the following areas:

- Geometry Modeling and Preparation for Meshing
- Fixed Grid RANS (meshing and CFD)
- Mesh Adaptation for RANS (meshing and CFD)
- High Order Discretization (meshing and CFD)

*Professor, Department of Mechanical Engineering. Fellow AIAA. mavripl@uwyo.edu

- Hybrid RANS/LES (meshing and CFD)
- Wall-Modeled LES and Lattice-Boltzmann (meshing and CFD)

The TFG approach was formulated in response to observations obtained from the previous HLPW3 workshop, which was held in 2017. Comparisons of the collective HLPW3 results with previous workshops concluded that the rate of progress in predictive ability of steady-state RANS methods for high-lift problems was slow or stagnating, and that new technologies needed to be brought to bear on the problem in order to accelerate progress. With this in mind, the motivation of the work reported in this paper was to compare the accuracy and performance of a traditional steady-state RANS approach with a novel hybrid RANS-LES methodology, which includes several advanced technological features.

The RANS approach used in this work is based on the NSU3D unstructured mesh solver. NSU3D was a participant in the first and second high-lift workshops, HLPW1 in 2010[1] and HLPW2 in 2013.[2] NSU3D has also been validated through participation in the first Aeroelastic Prediction workshop[3] and the majority of the Drag Prediction Workshop series.[4] The hybrid RANS-LES methodology employs a dual-solver paradigm implemented through overset near-body/off-body meshes, similar to codes such as HELIOS.[5] In this approach, NSU3D is used as the near-body solver operating on body fitted unstructured meshes, while the off-body solver employs a high-order accurate discontinuous Galerkin discretization on hexahedral meshes. Furthermore, the off-body meshes employ dynamic adaptive mesh refinement (AMR), enabling higher resolution in critical regions of the flow-field. While the RANS results presented in this paper fall in the domain of the Fixed Grid RANS TFG, the hybrid RANS-LES results include elements of interest to multiple TFGs, including the AMR TFG, High-order discretizations, and Hybrid RANS/LES. The two approaches presented in this paper offer the possibility of comparing the hybrid RANS/LES simulations with the RANS results obtained using the same RANS solver in both approaches running on the same near-body meshes. Finally, it should be noted that the results presented in this paper were not included as part of the HLPW4 workshop collective results reported at the workshop or included in the summary papers, since the hybrid RANS-LES results were not completed in time for the submission deadline.

In the following section, a brief description of the RANS and hybrid RANS-LES methodologies is given. This is followed by a presentation of the results obtained with NSU3D alone for fixed grid RANS computations. Next, the results for two cases using the hybrid RANS-LES approach are given and compared with the former results. Conclusions on accuracy and efficiency of the two approaches are given along with plans for future work.

II. Solver Description

II.A. RANS Solver

The NSU3D code is an unstructured mesh multigrid Reynolds-averaged Navier-Stokes (RANS) solver for high-Reynolds number external aerodynamic applications. The NSU3D discretization employs a vertex-based approach, where the unknown fluid and turbulence variables are stored at the vertices of the mesh, and fluxes are computed on faces delimiting dual control volumes, with each dual face being associated with a mesh edge. This discretization operates on hybrid mixed-element meshes, generally employing prismatic elements in highly stretched boundary layer regions, and tetrahedral elements in isotropic regions of the mesh away from the aircraft surfaces. A single edge-based data-structure is used to compute flux balances across all types of elements. The convective terms are discretized as central differences with added matrix dissipation. Second-order accuracy is achieved by formulating these dissipative terms as an undivided bi-harmonic operator, which is constructed in two passes of a nearest-neighbor Laplacian operator. In the matrix form, this dissipation is similar to that produced by a Riemann solver gradient-based reconstruction scheme, and is obtained by replacing the difference in the reconstructed states on each side of the control volume interface by the undivided differences along mesh edges resulting from the biharmonic operator construction. These differences are then multiplied by the characteristic matrix to obtain the final dissipation terms. A Roe upwind scheme using least-squares gradient reconstruction is also available in the NSU3D solver, although this option has not been used in the present study. Previous work has shown that the matrix dissipation and Roe schemes in NSU3D give very similar results for subsonic and transonic flows, with the matrix dissipation scheme being slightly less diffusive overall in these flow regimes.

The baseline NSU3D discretization employs a finite-difference scheme to approximate the thin-layer form of the viscous terms for the Navier-Stokes equations, although this is done in a multidimensional fashion, by

computing a Laplacian of the velocity field. The main approximation in this approach is the omission of the cross-derivative viscous terms, and the assumption of a locally constant viscosity. The discretization of the full Navier-Stokes terms has also been implemented using a two-pass edge-based loop approach, although this option has not been used in the present study.

The current work uses the basic Spalart-Allmaras (SA) turbulence model (no QCR) following the implementation devised for avoiding negative eddy viscosity values, as described in reference.[6] The basic solver employs a line-implicit method, which is used as a smoother on fine and coarse levels of an agglomeration multigrid solver.[7] This basic solver strategy can be employed directly as an iterative nonlinear solver, or as a linear preconditioner for use in a Newton-Krylov method. NSU3D has been well validated for low-speed and transonic cruise problems as a regular participant in the AIAA High Lift Prediction Workshop (HLPW) series[8] and the Drag Prediction Workshop (DPW) series.[4] The unstructured prism-tetrahedral Pointwise meshes provided by the workshop were used for the NSU3D fixed-grid RANS calculations.

II.B. Hybrid RANS-LES Solver

The hybrid RANS-LES methodology is based on a dual-solver overset mesh paradigm. In this approach, the NSU3D RANS solver is used in near-body regions on the same workshop provided prism-tetrahedral unstructured meshes employed for the steady-state RANS results described in this paper. However, prior to computation, these meshes are trimmed by removing all mesh elements that are a prescribed distance away from the body. In this work the meshes were trimmed to a distance of 8 inches from the nearest body surface. The resulting near-body meshes are then overset with a background Cartesian mesh of variable resolution which supports the discretization of the off-body solver `dg4est`.[9,10] This solver is a combination of the nodal Discontinuous Galerkin (DG) solver CartDG[11–13] coupled with the dynamic adaptive mesh refinement framework `p4est`.[14] The numerical kernel, CartDG, discretizes the compressible full Navier–Stokes equations and implements the constant Smagorinsky Subgrid-Scale (SGS) model for turbulence.[15] To improve the numerical stability of the DG method, CartDG's formulation is based on a split-form flux scheme possessing the summation-by-parts property to mimic integration-by-parts discretely.[16] To achieve high computational efficiency, CartDG exploits simplifications in Cartesian mesh settings and utilizes a tensor-product, collocation-based DG method. This enables the use of very high orders of accuracy (i.e. up to 8^{th} order in reference[17]).

The p4est AMR framework[14] is based on a distributed octree approach which provides cell-size or h-adaptation. In addition, a p-refinement capability is incorporated by offloading and managing variable data sizes which allows each cell to have a variable polynomial degree. CartDG employs a p-adaption strategy for the off-body solver that favors low polynomial degrees and fine meshes where the off-body is in close proximity to the near-body, and high polynomial degrees away from the near-body. The p-adaption strategy for the off-body solver can be summarized with these five rules:

- Refine and match the off-body resolution both in mesh size and order of accuracy with that of the near-body mesh in close proximity to the overlap region of the overset grids.
- Increase the polynomial degree in the off-body region as quickly as possible without creating a more restrictive time step by simultaneously increasing the mesh size and raising the polynomial degree of the discretization.
- Refine the mesh to flow features using the highest possible polynomial degree.
- Ensure maximum 2:1 refinement jumps and p+1:p order of accuracy jumps between neighboring cells through additional refinement passes.
- Refine elements to stay ahead of propagating flow features. This is implemented by refining any neighboring cells that share a face with a cell that has been tagged for flow feature refinement. To detect a flow feature, the solution gradients are used, and the Q criterion is calculated at the quadrature points of the high-order discretization in each mesh cell. If the Q criterion at a quadrature point is greater than a tolerance τ, then the cell is tagged for refinement.

The overset interpolation patterns between the near-body and off-body meshes are computed using the Topology Independent Overset Grid Assembly (TIOGA) library, which provides interpolation accuracy consistent with the discretization order of accuracy.[18] TIOGA employs a fast distributed ADT search to determine

the overset grid interpolation patterns and is used in a dynamic fashion at each global time step. Although the current high-lift aerodynamic simulation cases do not contain any relative grid motion, the overset interpolation patterns must still be recomputed at each time step due to the dynamically changing refinement patterns in the off-body mesh.

In the context of dynamic overset grid simulations paired with NSU3D as a near body solver, `dg4est` has been validated for large-scale wind energy problems,[19–21] rotorcraft[22] applications, and for the Workshop for Integrated Propeller Prediction (WIPP) test cases.[23]

III. RANS Results

For the fixed-grid RANS cases, the "Pointwise Unstructured Smoothed" prism-tet dominant meshes supplied by the workshop were used. Four levels of grid densities were provided by the workshop committee ranging from coarse (level A) to very fine (Level D) and their statistics are presented in Figure 1. The typical

Level	#Tetra	#Pyra	#Prism	#Cells	#Nodes	Estimated wall y+ values
A	8,252,688	283,581	20,580,545	29,116,814	11,943,153	2.25
B	18,606,040	496,238	56,170,207	75,272,485	31,660,032	1.50
C	47,208,155	957,470	164,287,274	212,992,899	91,112,700	1.00
D	96,371,306	1,657,058	370,449,431	372,106,489	202,542,838	0.75

Figure 1. Grid statistics of the four different densities grids used in this work provided by the workshop.

sequence for computing the test cases was to start the CFD simulations using a 3-level multigrid convergence acceleration technique. Once the flow was established, the final iterations were carried out in the absence of multigrid on the single fine grid. For cases with flow separation that may not fully converge, the final fine grid iterations allow for lower final residual tolerances. As expected, convergence of the CFD simulations became slower with increasing mesh density. Figure 2 shows the overall convergence of the residuals of the density for Level A, B, C and D grids and the lift coefficient for typical engineering simulations. The initial residual transients correspond to grid sequencing, where the initial solution is first computed on coarse levels and interpolated recursively to the finest level. Thereafter, the multigrid algorithm is used to drive the residuals down over the next 2000 cycles, after which the solver switches to single fine grid iterations. The lift converges typically to acceptable tolerances within less than 5000 iterations. For cases with more flow separation and unsteady behavior, force and moment coefficient histories are typically averaged in pseudo-time. However, for the workshop cases, an investigation was carried out to study the extent of convergence that could be obtained on these progressively finer meshes. For this study, calculations were run out to much longer time histories using up to 75,000 cycles as illustrated in Figure 3 through 5 where from the left to right, the convergence of the last iterations are displayed of the lift coefficient, the drag coefficient and the pitching moment coefficient respectively for the nominal case i.e. Mach $= 0.20$, $\alpha = 7.05^o$, $Re_{\texttt{MAC}} = 5.67$ million, $\delta_{flap_{INB}} = 40^o$, $\delta_{flap_{OUTB}} = 37^o$. Figure 3 shows the convergence behavior of the coefficients on grid Level A where all oscillations are converging. The variation of e.g. the drag coefficient over the last 5000 iterations is 0.39 drag counts. The dashed lines show the averaged values for each coefficient and these values were used as final results. Similar convergence plots are shown for grid Level B in Figure 4. Note that the oscillations are still converging but the convergence is slower and requires more iterations. The variation for the drag coefficient is 1.03 drag count for the last 10,000 iterations. The calculations were stopped at this point. Figure 5 shows the convergence behavior of the Level C grid. The oscillations are not converging but stay bound between the same levels. The variation of the drag coefficient over the last 10,000 iterations varies 9.42 drag counts. On the Level D grid, a fully converged solution could not be obtained and also here, average values were taken. Although NSU3D includes a Newton-Krylov solver that is often capable of converging difficult problems to machine zero, this option was not exercised in this study in the interest of conserving computational resources. From past experience,[24,25] we speculate that the Newton-Krylov solver would be able to achieve machine zero on grids A and B, although the cost for grids C and D may be excessive.

The increasing resolution of surface flow features on the wing can be clearly observed in Figure 6 where the y^+ values are displayed for the nominal case for the four different grid levels. In Figure 1, the estimated

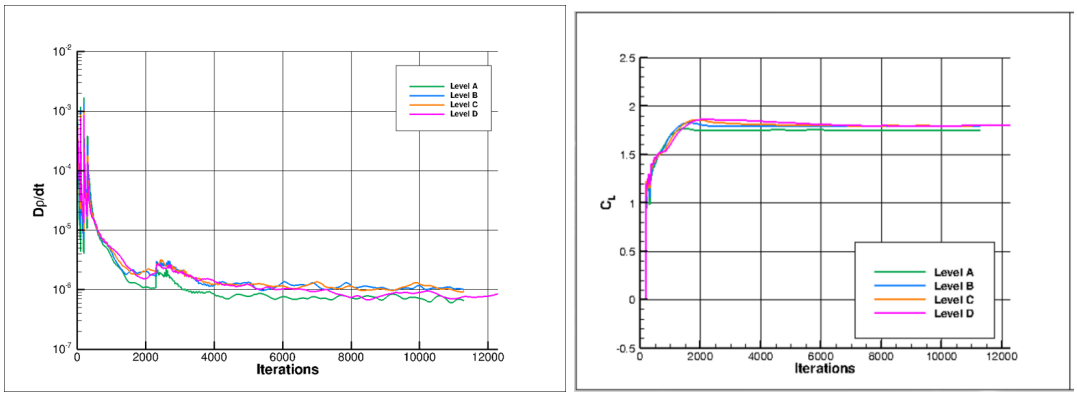

Figure 2. Residual convergence (left) and CL convergence (right) for all 4 grid levels for the nominal case i.e. Mach = 0.20, $\alpha = 7.05^o$, $Re_{\text{MAC}} = 5.67$ million, $\delta_{flap_{INB}} = 40^o$, $\delta_{flap_{OUTB}} = 37^o$.

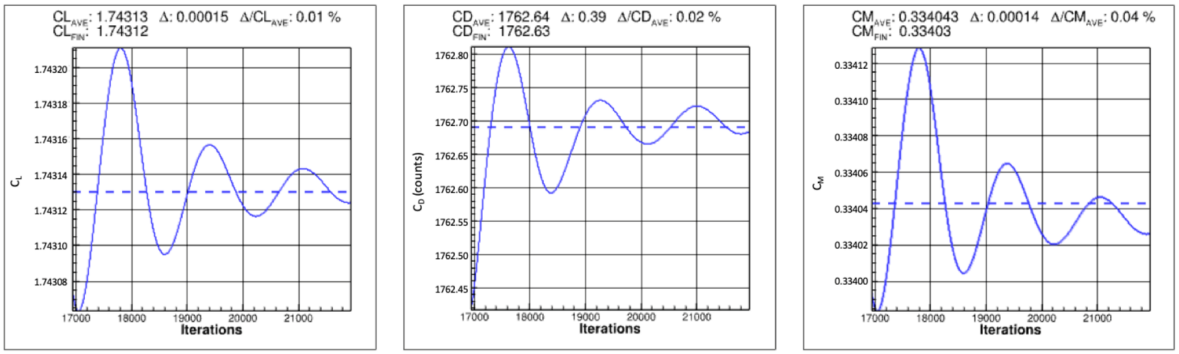

Figure 3. Long time asymptotic convergence behavior of the lift coefficient (left figure) the drag coefficient (middle figure) and the pitching moment coefficient (right figure) for Level A grid.

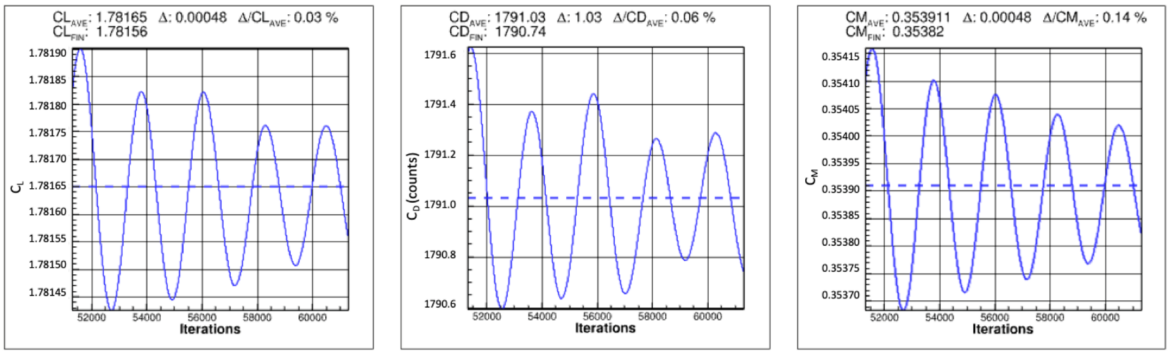

Figure 4. Long time asymptotic convergence behavior of the lift coefficient (left figure) the drag coefficient (middle figure) and the pitching moment coefficient (right figure) for Level B grid.

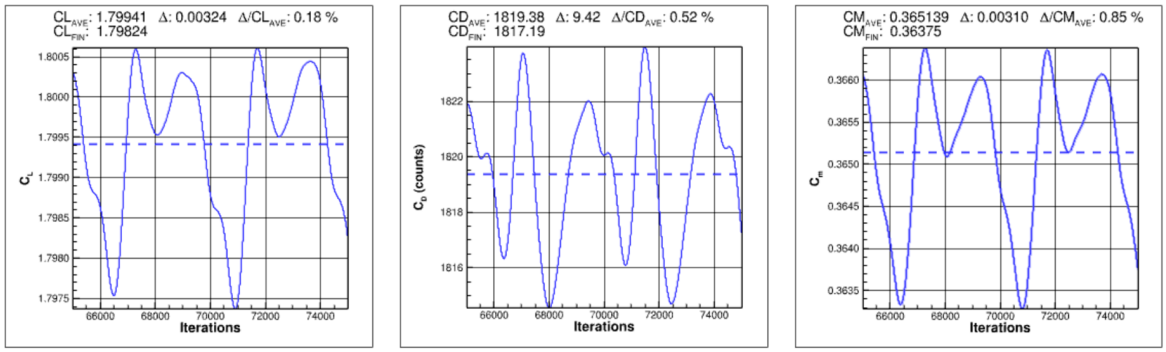

Figure 5. Long time asymptotic convergence behavior of the lift coefficient (left figure) the drag coefficient (middle figure) and the pitching moment coefficient (right figure) for Level C grid.

y^+ values are specified and the results show that the design intent of the grids is indeed satisfied. The effect of the slat track brackets on the flow can clearly be observed by the dark streaks coming from the leading edge and their definition becomes more refined with increasing grid density.

III.A. Case 1a: Flap Deflection Study

For this study, two additional flap deployments were added namely $\delta_{flap_{INB}} = 37^o$, $\delta_{flap_{OUTB}} = 34^o$ and $\delta_{flap_{INB}} = 43^o$, $\delta_{flap_{OUTB}} = 40^o$. Figure 7 shows the surface skin friction stream lines for the three different configurations. The red colors indicate areas where the x-component of the skin friction coefficient (i.e. C_{f_x}) becomes negative and is thus an indication of reversed flow on the surface due to flow separation. The unsteady nature of the separation can be seen as red pockets are formed on the outboard flaps. Figure 8 shows the incremental lift coefficient, drag coefficient and pitching moment with respect to the nominal configuration. All results were obtained on the finest grid level i.e. Level D. The values lie within the range of all participants of the HLPW4. Note that, contrary to expectation and experimental data from the workshop, the highest flap deflection does not produce the highest lift coefficient. This effect was observed by the majority of workshop participants and is attributed to the increasing amount of flow separation as was shown in Figure 7.

III.B. Case 1b: Grid Convergence Study

The grid refinement study is presented in Figure 9. On the x-axis is the grid factor defined as $\frac{1}{N^{\frac{2}{3}}}$ where N represents the total number of grid points. For a second-order accurate discretization, a linear relationship between the discretization error and grid factor is expected. Although results on the first three grids line up well on these plots, the finest mesh shows a deviation from this linear progression. This may be attributed to time-averaging of the final results and/or nonlinearities introduced by increased flow separation. The experimental results are presented as a dashed line in the three graphs. The lift coefficient is slightly overpredicted compared the experimental results by 0.019 (1.1%) while the drag coefficient is overpredicted by 42.4 drag counts (2.3%) and the pitching moment is underpredicted by 0.0059 (i.e. 1.6%). These values are in line with the bulk of the participants of the HLPW4.

III.C. Case 2a: $C_{L_{max}}$ Study

Full polars were run on Level C and Level D mesh and compared to experimental results from the Qinetiq five-meter pressurized low-speed wind tunnel. With the exception of the pitching moment, the comparison with the experimental results, presented in Figures 10 is good. In general, the difference between Level C and Level D grids is very small. Figure 11 illustrates additional details in the region near $C_{L_{MAX}}$. The results on the level D mesh are closer to the experimental values while the results on the level C mesh are slightly overpredicted. Note that no suitably steady-state results could be obtained on level D mesh beyond an angle of attack 19 degrees. Wing pressures are compared between the NSU3D code and the wind-tunnel results from Qinetiq for the nominal case M = 0.20 $\alpha = 7.05^o$, $Re_{\texttt{MAC}} = 5.67$ million on all four mesh levels. The inboard and outboard cuts are presented in Figure 12 and Figure 13 respectively. The pressure comparison

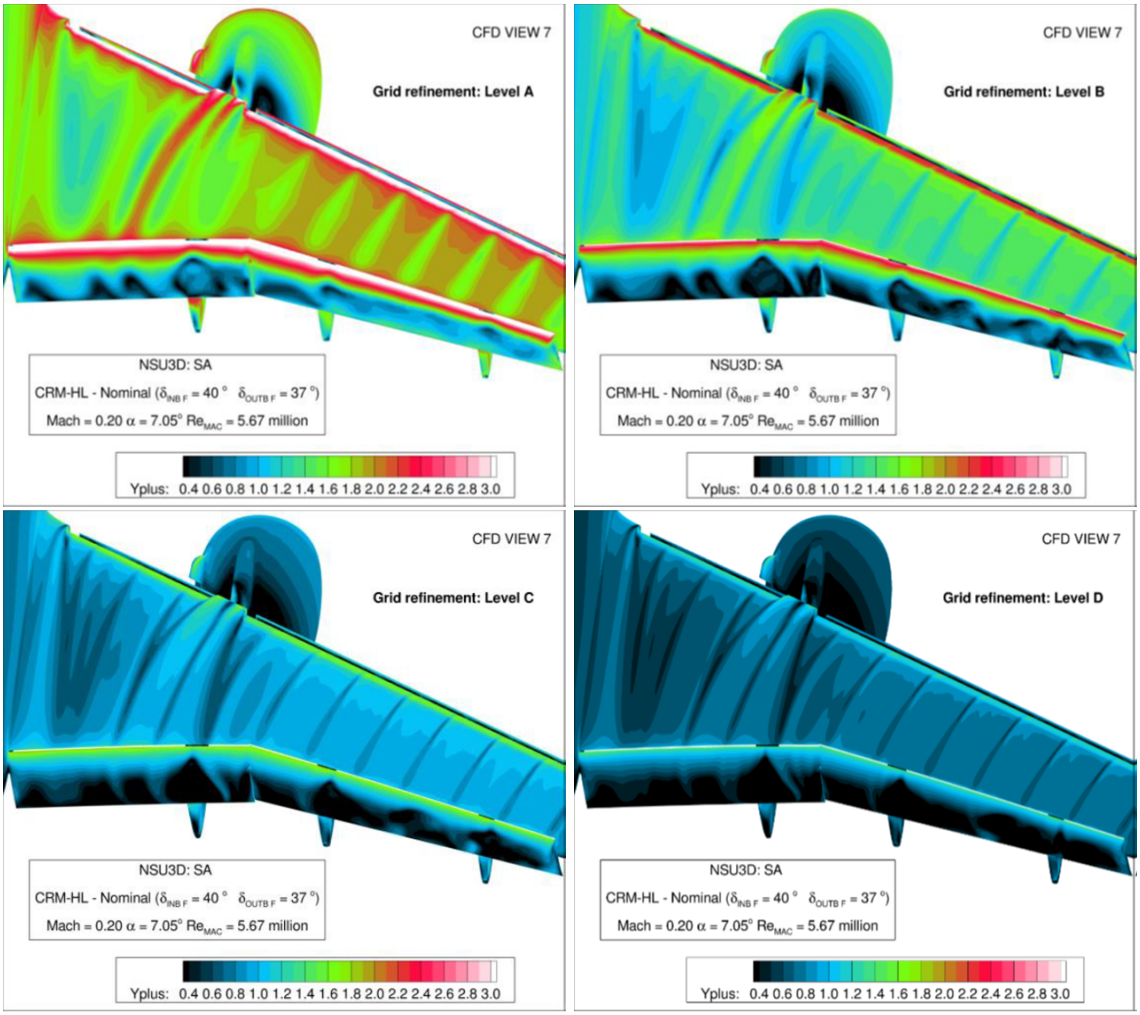

Figure 6. y^+ **values for the nominal case for level A grid (top left), level B grid (top right), level C grid (bottom left) and level D grid (bottom right).**

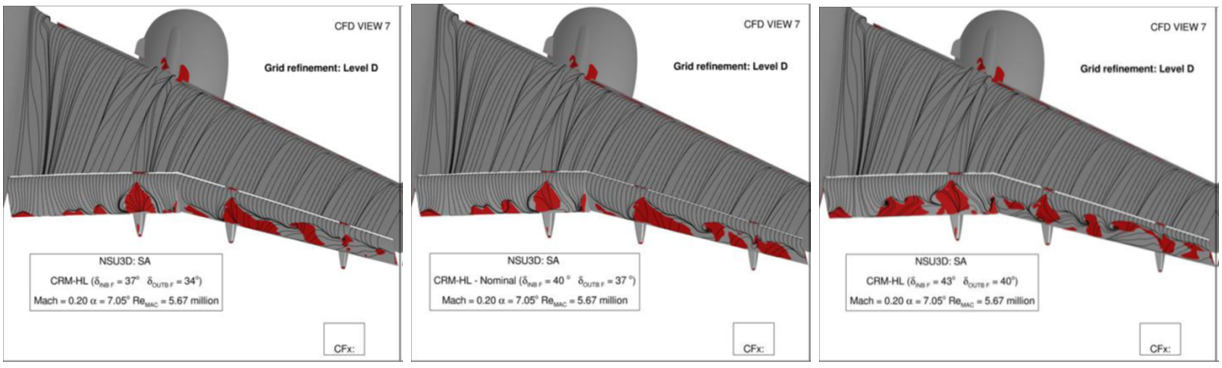

Figure 7. Skin friction lines and regions of flow separation in red of the nominal case for $\delta_{flap_{INB}} = 37^o$ - $\delta_{flap_{OUTB}} = 34^o$ (left figure), $\delta_{flap_{INB}} = 40^o$ - $\delta_{flap_{OUTB}} = 37^o$ (middle figure), and $\delta_{flap_{INB}} = 43^o$ - $\delta_{flap_{OUTB}} = 40^o$ (right figure).

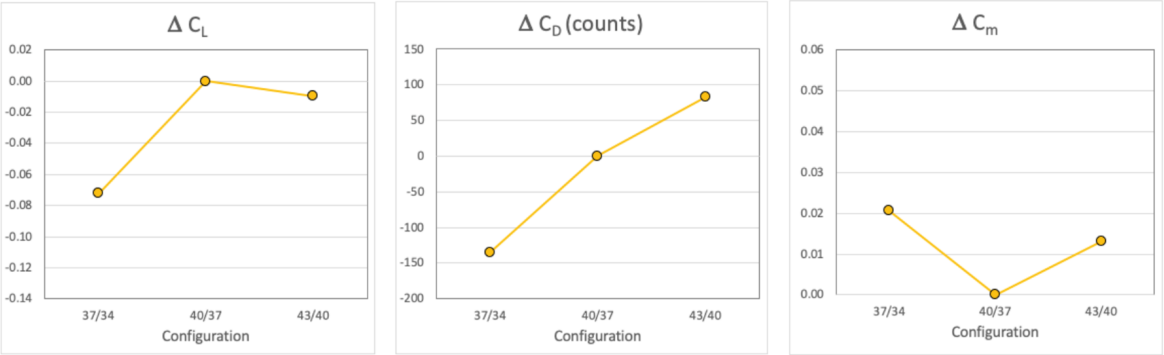

Figure 8. Flap deflection study incremental lift (left figure), incremental drag (middle figure) and incremental pitching moment with respect to the nominal configuration ($\delta_{flap_{INB}} = 40^o$ - $\delta_{flap_{OUTB}} = 37^o$) for Mach = 0.20, $\alpha = 7.05^o$, $Re_M AC$ = 5.67 million

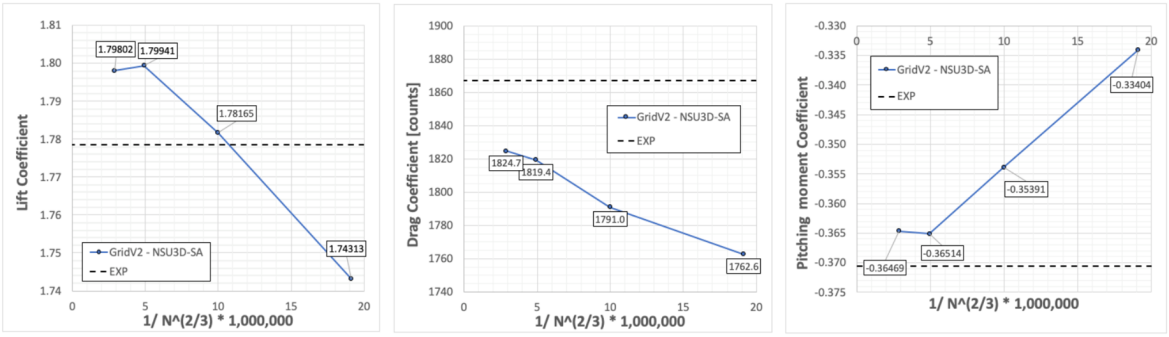

Figure 9. Lift-, Drag- and Pitching moment coefficient as function of the grid resolution factor

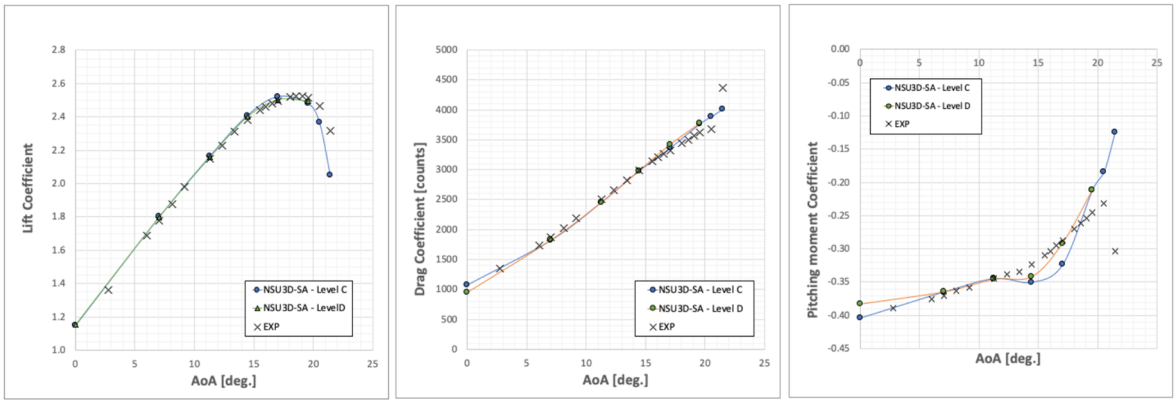

Figure 10. Lift-, Drag- and Pitching moment coefficient as function of the angle of attack at Mach = 0.20 Re_{MAC} =5.67 million.

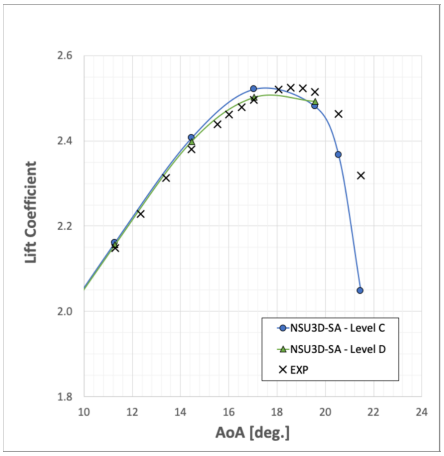

Figure 11. Lift coefficient as function of the angle of attack near stall at Mach = 0.20 Re_{MAC} =5.67 million.

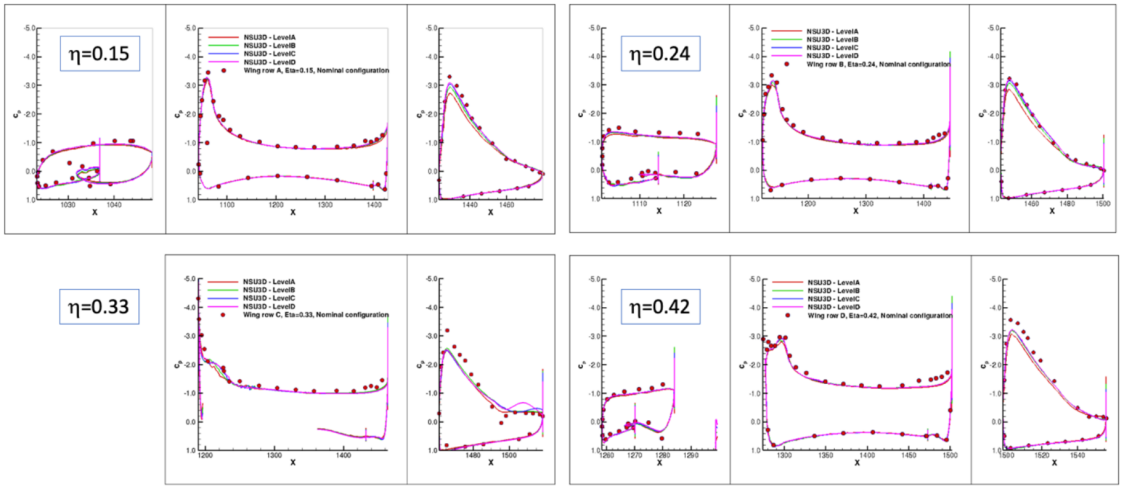

Figure 12. Inboard wing pressure cut comparison between NSU3D and experimental data from Qinetiq at M = 0.20 $\alpha = 7.05^o$, Re_{MAC} = 5.67 million.

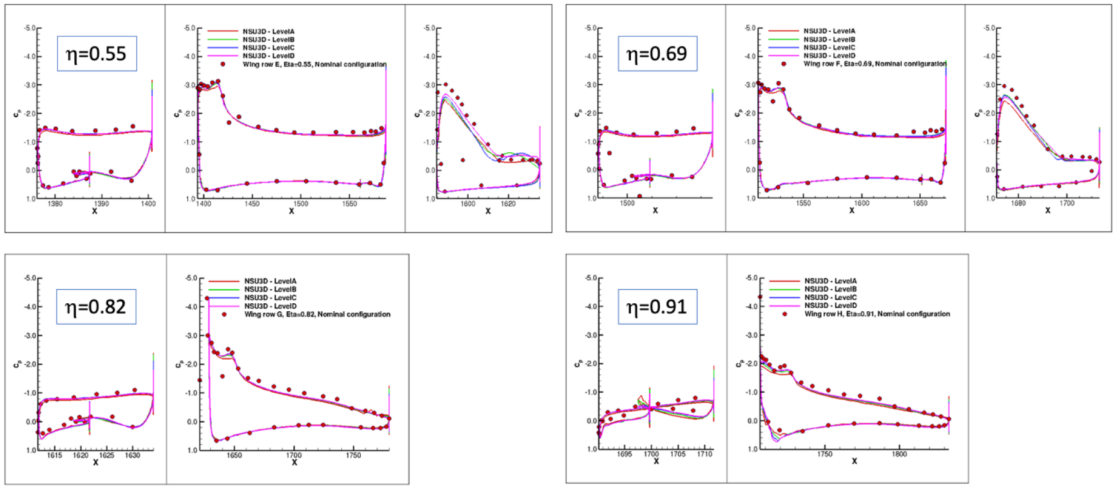

Figure 13. Outboard wing pressure cut comparison between NSU3D and experimental data from Qinetiq at M = 0.20 $\alpha = 7.05^o$, Re_{MAC} = 5.67 million.

on the slats and the main element is in general well captured by the NSU3D code, while on the flaps, the suction peaks are slightly under-predicted. Note that the difference between the four grid levels is most noticeable on the flaps: the more the grids are refined, the closer the results match the experimental data. This significant difference in results between the different grid levels on the flaps suggests that the initial grid density on the flaps is somewhat too coarse. Note that at $\eta = 0.91$ the difference in grid density is noticeable on the lower surface of the main element. Contrary to the flaps, where results with increased mesh refinement approach the experimental data, at this outboard station, results with increasing mesh refinement move away from the experimental data in a small region on the lower surface of the wing.

The wing pressures are also compared near stall at $\alpha = 19.57^o$ and are presented in Figure 14 and Figure 15. Similar observations can be made: the pressures on the slats and the main element are well captured while on the flaps larger discrepancies are noted. At the two most outboard sections (i.e. $\eta = 0.82$ and $\eta = 0.91$), there is evidence of significant difference with the experimental data. This is attributed to overprediction of the region of separated flow on the outboard wing at these conditions compared to experimental data.

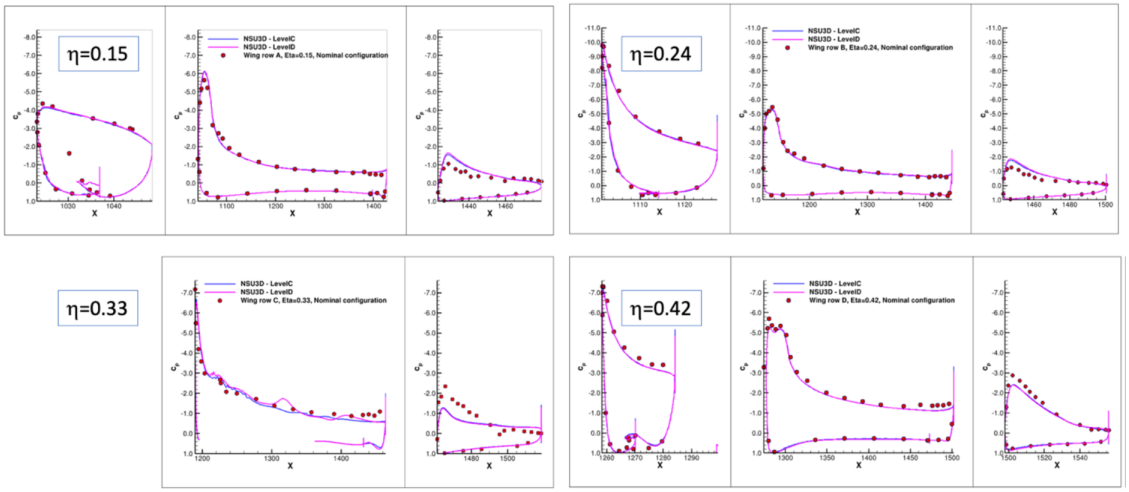

Figure 14. Inboard wing pressure cut comparison between NSU3D and experimental data from Qinetiq at M = 0.20 $\alpha = 19.57^o$, Re_{MAC} = 5.67 million.

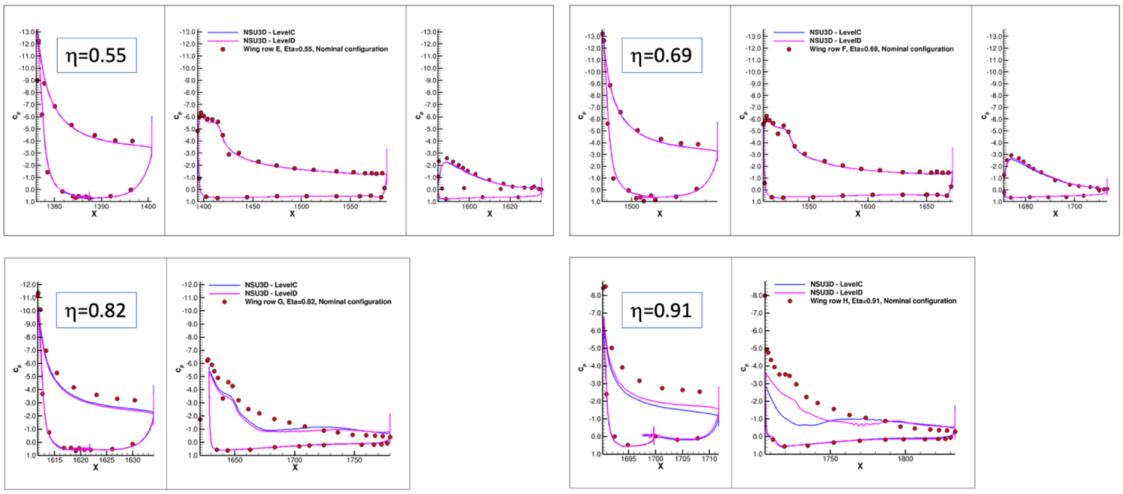

Figure 15. Outboard wing pressure cut comparison between NSU3D and experimental data from Qinetiq at M = 0.20 $\alpha = 19.57^o$, Re_{MAC} = 5.67 million.

A comparison between skin friction lines predicted by the NSU3D code and oil flow images from experimental results from Qinetiq are shown for pre-stall (Figure 16) conditions and post-stall (Figure 17) conditions. For the pre-stall condition, the similarities in flow phenomena between the NSU3D and the

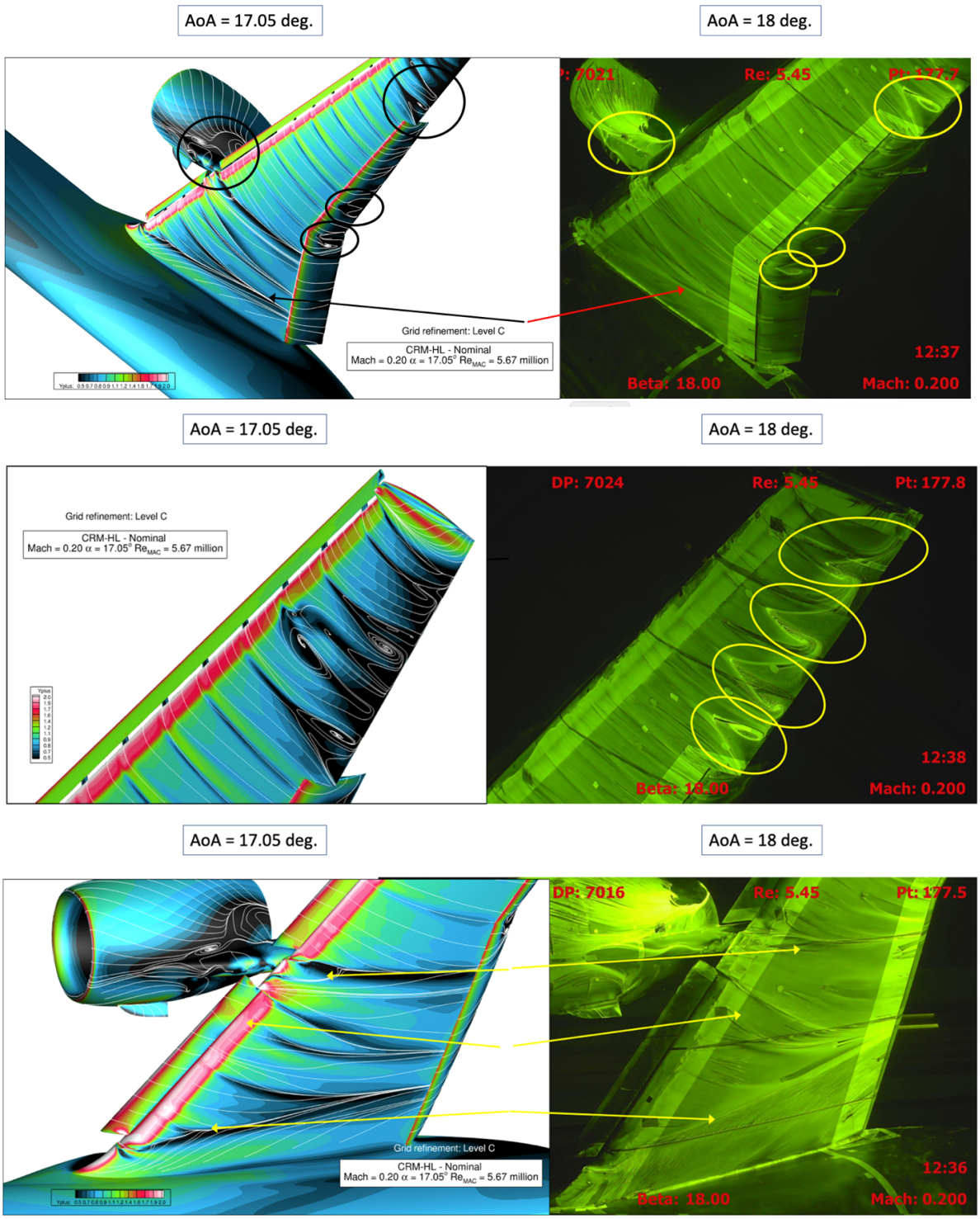

Figure 16. Comparison of flow visualization between NSU3D and experimental data from Qinetiq M = 0.20 $\delta = 17.05^{o}$, Re_{MAC} = 5.67 million.

experimental data can clearly be seen and are highlighted by the circles on the images. Notably the localized regions of separation on the outboard wing, mid-flap locations, and nacelle-pylon region appear to be captured qualitatively. In the post-stall condition (Figure 17) there are significant differences in flow patterns. The outboard wing section is more massively separated in the RANS simulations compared to experimental data as seen in the figure and evidenced from the C_p plots discussed above. Additionally, in the inboard

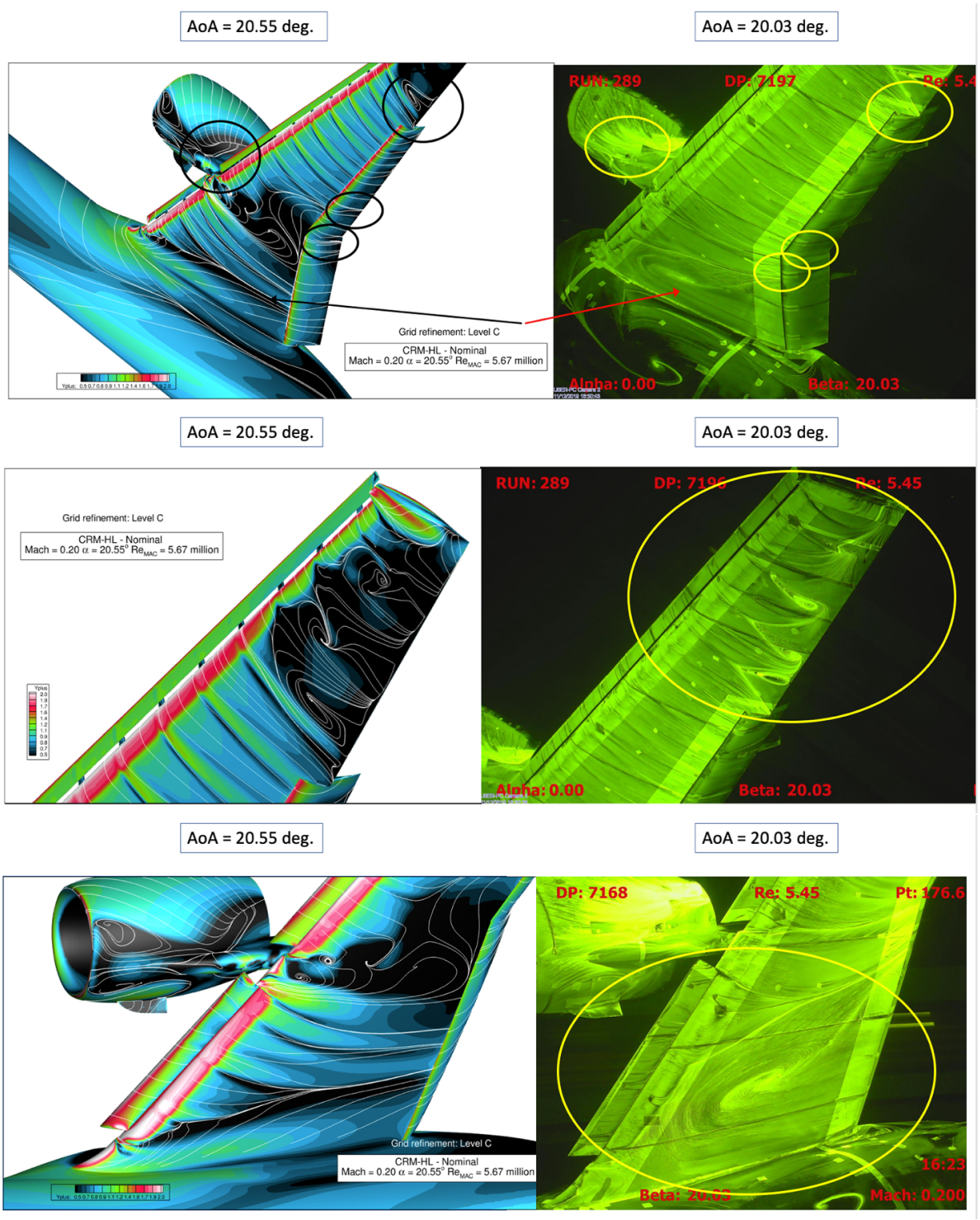

Figure 17. Comparison of flow visualization between NSU3D and experimental data from Qinetiq at M = 0.20 $\delta = 20.55^o$, Re_{MAC} = 5.67 million.

region near the fuselage, the CFD simulation predicts mostly attached flow, whereas the experimental flow images clearly show evidence of massive flow separation on the wing and on the fuselage. Due to the nature of the RANS methodology, this massive flow separation is not predicted correctly. We also note the the current simulations do not incorporate the QCR correction for the Spalart-Allmaras turbulence model, as mentioned previously.

IV. Hybrid RANS-LES Results

The hybrid RANS-LES approach is applied to the `Case 2a:` $C_{L_{max}}$ study for two inflow conditions of 7.05° and 21.47° angles of attack in a free air setting. Simulations are initiated from freestream conditions (cold start) and simulated for 30 Convective Time Units (CTU), defined as the time for freestream flow to travel the distance characterized by the Mean Aerodynamic Chord. The near-body solver NSU3D employs the implicit 2$^{\text{nd}}$-order Backwards Difference Formula (BDF2) method for temporal discretization, while the off-body solver `dg4est` employs the explicit 3-stage Strong-Stability Preserving 3$^{\text{rd}}$-order Runge-Kutta (SSP-RK3) time stepping method. A non-dimensional time step size of 1.8×10^{-4} is chosen which is approximately 5.5x smaller than the estimated dominant turbulent time scale.

The near-body solver utilizes the same Level-C mesh used for the steady-state RANS simulations but trimmed to a distance of 8 inches from the nearest body. This mesh is overset with a dynamically adaptive background Cartesian mesh with a maximum resolution of 1.9 inches in a free-air domain spanning 10^6 inches in each coordinate direction, resulting in 16 levels of h-refinement[1] as shown in Fig. 18(a). Additionally, a stream-wise slice of the off-body mesh near the wing-tip is shown in Fig. 19 illustrating the refinement for capturing the wing-tip vortex. Each mesh level is assigned a spatial discretization solution polynomial degree (`p-degree`): Level 0 contains `p2` elements, Level 1 contains `p3` elements, and Levels 2-15 contain `p5` elements. The solution order of accuracy is `p`+1, e.g., `p5` is 6$^{\text{th}}$-order accurate asymptotically. Adaptive mesh refinement is performed at an interval of 10 time steps whereby refining and coarsening of mesh elements occurs controlled by solution feature-based tagging. The initial off-body mesh for each case contains 1.2 million elements and 100 million degrees-of-freedom (DOF). The mesh grows rapidly to 9.1 million elements and 290 million DOF after the initial simulation transient and remains approximately constant thereafter due to a high-threshold feature value criterion. Figure 18(b) illustrates the iso-contour of vorticity magnitude for the overset HRLES simulation for the 7.05° case.

Force coefficient histories for the 7.05° case are shown in Fig. 20. Large variations occur during the initial transient phase up to 8 CTU. Additionally, a large transient event occurs at approximately 17-19 CTU, highlighting a significant drop and recovery in the lift and spike in the pitching moment. Subsequently, temporal-averaged force coefficients are computed from data acquired during 20-30 CTU, indicated by the bold profiles in the figure, and tabulated with the RANS and experimental results in Table 1. In comparison to the RANS results, the HRLES results generally perform better for the prediction of C_L and C_D as compared to experimental data, whereas CM_{Pitch} is better predicted by the RANS model for the 7.05° case. Figure 21 shows the force coefficient temporal histories for the 21.47° case and, additionally, compiled in Table 1. Similar to the lower angle of attack case, initial transients occur over the first 12 convective time units. Temporal averaging for HRLES force coefficients are initiated at 12 CTU and continued until the simulation terminates at 30 CTU. In contrast to the 7.05° case, the variances in the statistics are much larger as the data contains large fluctuations. This is expected as much larger flow separation dynamics occur at higher angles of attack. Figure 22 displays instantaneous `Y+` values for the 7.05° and 21.47° cases on the wing surface. The flow behaves well across the planform at the lower angle of attack, contrasting to the high angle of attack exhibiting large flow separations inboard, from the fuselage to the midboard flap, and at the outboard as seen in Fig. 23. The excessive outboard wing separation attributes to the lift, drag, and moment losses for our hybrid RANS-LES simulation results but to lesser extent than the steady-state RANS results shown in Fig. 17.

Case2a: **7.05°**	C_L	C_D	CM_{Pitch}
RANS	1.79941	0.18194	-0.36514
HRLES	1.78917	0.18907	-0.34665
Experiment	1.77862	0.18671	-0.37060

Case2a: **21.47°**	C_L	C_D	CM_{Pitch}
RANS	2.040316	0.399975	-0.133235
HRLES	2.217030	0.407150	-0.178867
Experiment	2.318240	0.436478	-0.303606

Table 1. Time-averaged simulation force coefficients and free-air corrected experimental data.

The hybrid RANS-LES simulations were performed on 5,400 2.3-GHz Intel Xeon E5-2697V4 (Broadwell) CPU cores. The near-body flow solver NSU3D utilized 3,600 cores while the remaining cores hosted the off-body solver `dg4est`. Each flow solver executed in parallel, taking approximately 4.5 seconds to simulate one time step. For each BDF-2 time step, the near-body solver used a 4-level linear agglomeration multigrid algorithm with 10 iterations. Figure 24 shows the iterative convergence comparison of the linear versus

[1] Level 0 (finest) - Level 15 (coarsest)

nonlinear multigrid algorithms on the CRM-HL test case using four mesh levels, justifying our use of the linear multigrid algorithm. For the same time-step size, the off-body solver required approximately 4 to 6 explicit SSP-RK3 steps. Overall, each cased used 37,200 cores-hours per CTU, though these results were not optimized for HPC performance or implicit time step convergence.

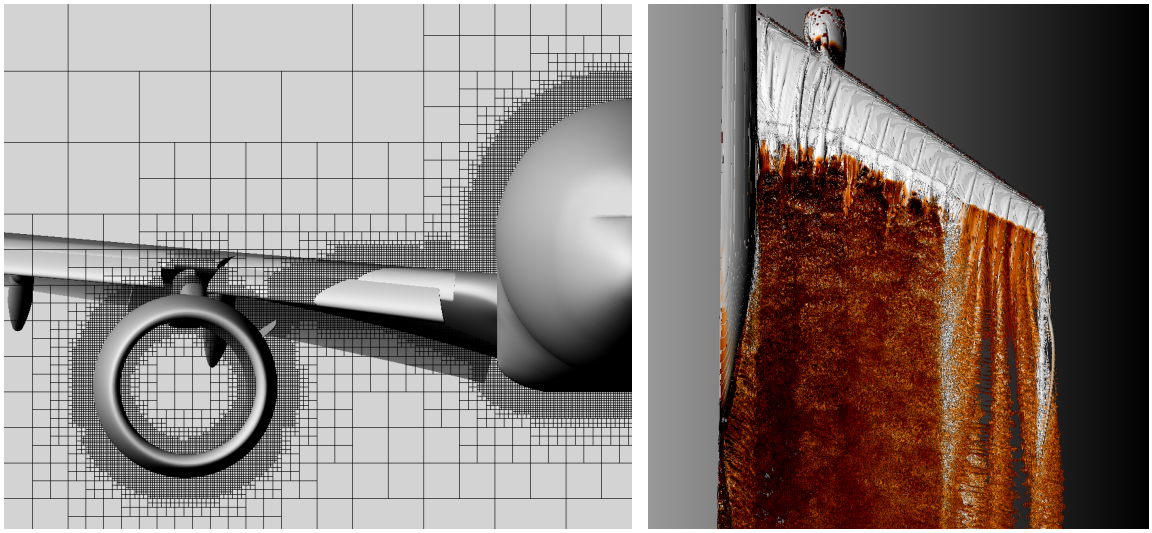

(a) Adapted off-body Cartesian mesh.

(b) Iso-contour of vorticity magnitude.

Figure 18. Overset RANS-LES simulation of the CRM-HL aircraft at 7.05° for Case2a.

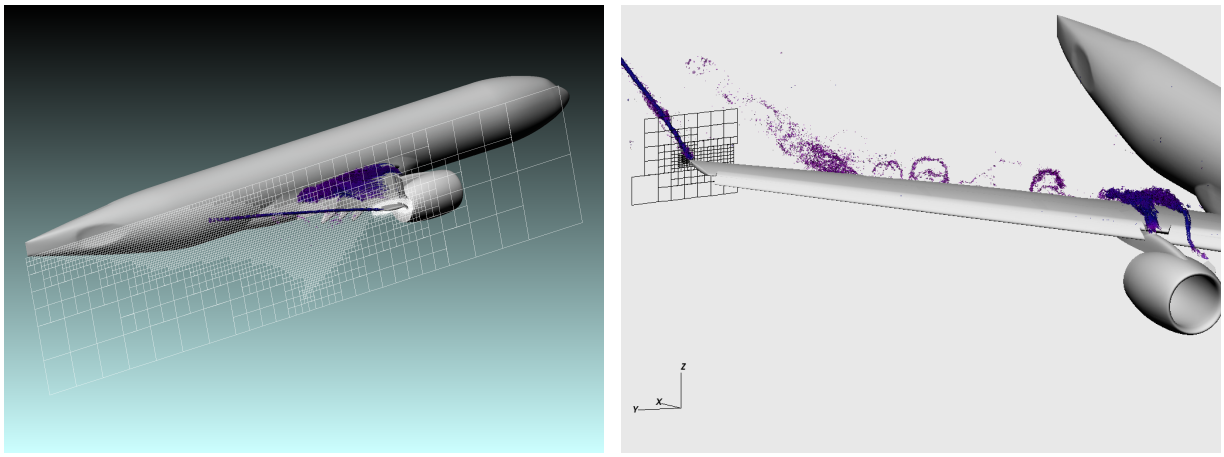

(a) Slice of adapted off-body Cartesian mesh in wake near the aircraft wing-tip.

(b) Wing-tip vortex with illustration of local mesh refinement.

Figure 19. Feature-based and inter-grid boundary-point adapted off-body Cartesian mesh with wing-tip vortex. Solution accuracy varies with mesh element refinement: 3^{rd}-order elements on finest mesh level, 4^{th}-order elements on the penultimate finest mesh level, and 6^{th}-order elements on all remaining mesh levels.

V. Conclusions

In this work, we have employed two methodologies for computing test cases defined for the fourth High-Lift Prediction Workshop. The first approach consists of a traditional fixed-grid RANS technique operating on unstructured grids. The results obtained fall largely within the average collective results reported by the fixed-grid RANS Technical Focus Group. Although $C_{L_{max}}$ is reasonably well predicted, discrepancies in the onset and patterns of flow separation are observed which in turn affect pitching moment predictions. These results for the RANS solver are not unexpected, given the experience from previous high-lift workshop

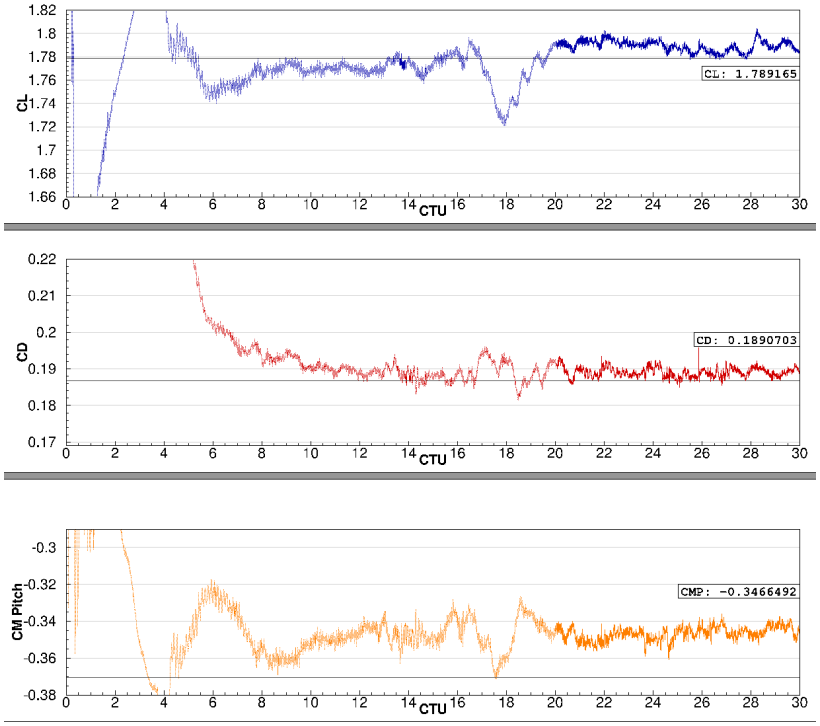

Figure 20. Force coefficients for the Hybrid RANS-LES simulation for angle of attack 7.05° case. The coefficients are time averaged over the solid line profiles starting at 20 CTUs. Solid black lines represent the experimental freestream corrected values provided by the Workshop.

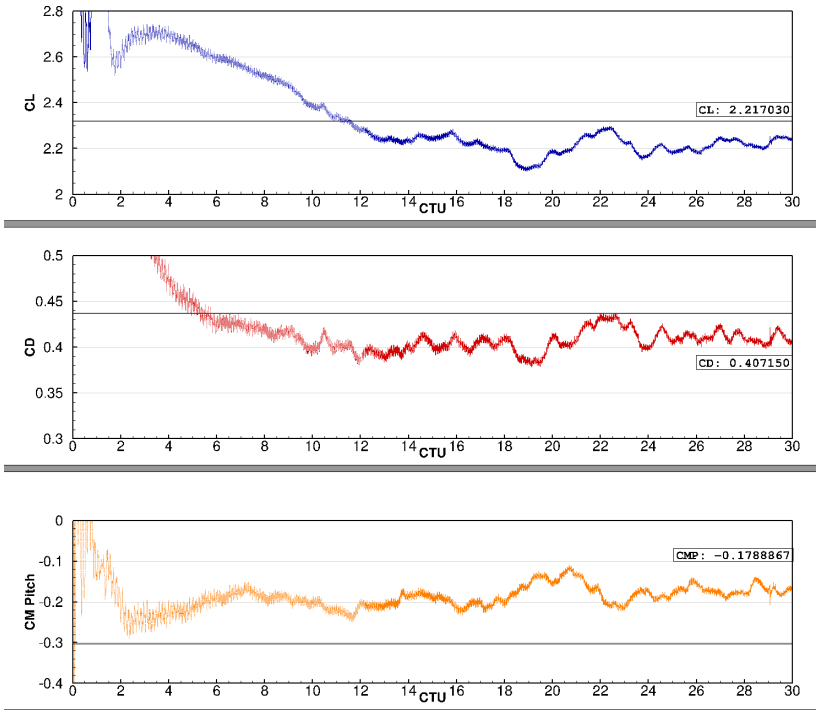

Figure 21. Force coefficients for the Hybrid RANS-LES simulation for angle of attack 21.47° case. The coefficients are time averaged over the solid line profiles starting at 12 CTUs. Solid black lines represent the experimental freestream corrected values provided by the Workshop.

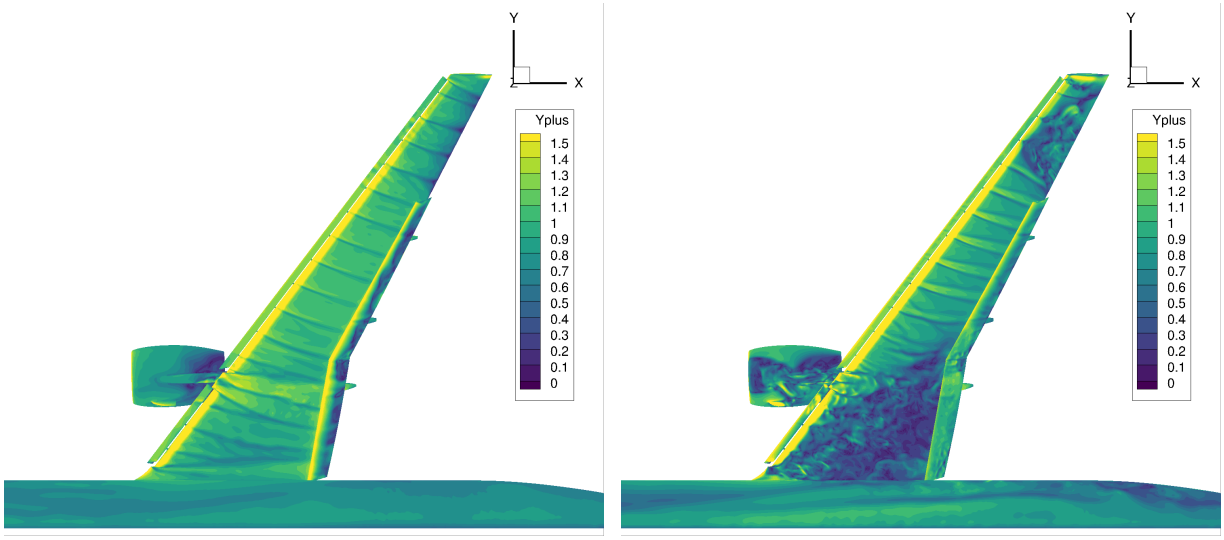

(a) 7.05° angle of attack. (b) 21.47° angle of attack.

Figure 22. Instantaneous Y+ profiles of the RANS-LES simulations of the CRM-HL aircraft for Case2a.

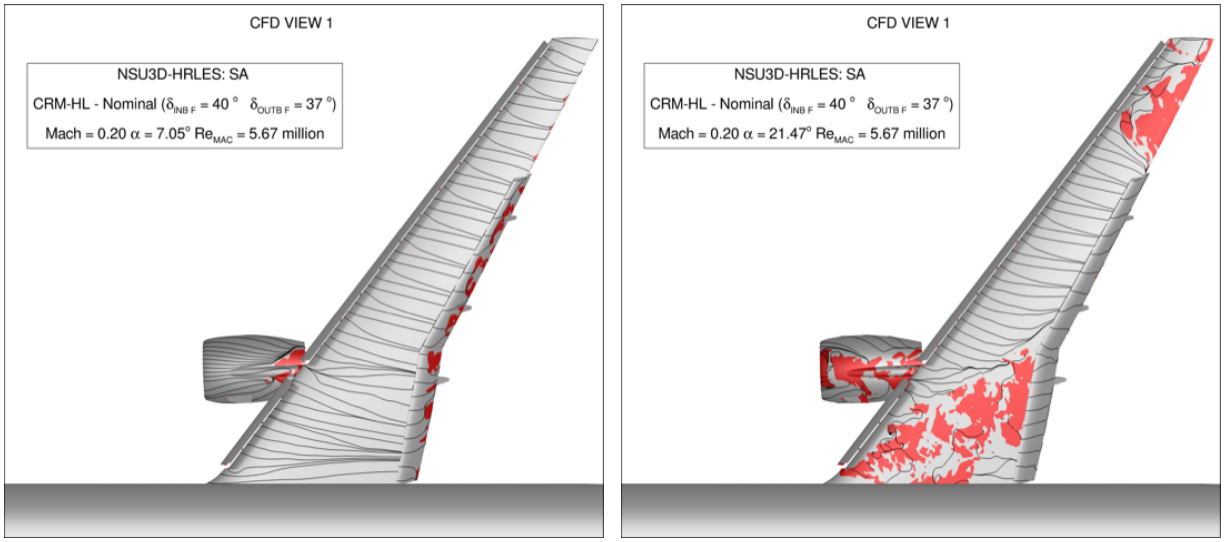

(a) 7.05° angle of attack. (b) 21.47° angle of attack.

Figure 23. Instantaneous streamlines and separation zones of the RANS-LES simulations of the CRM-HL aircraft for Case2a.

results. The hybrid RANS-LES simulations show improved force and moment predictions in the post-stall region, although the magnitude of the pitching moment is still underpredicted. The hybrid RANS-LES simulations come at a much higher cost but offer the potential for improved accuracy for problems with flow separation. The approach adopted herein combines several advanced technologies including high-order low dissipation discretizations and dynamic adaptive mesh refinement in both cell size (h) and discretization or p-order. However, much work remains to investigate and optimize the current hybrid approach including grid and time step resolution as well as adaptive meshing criteria. For static-geometry high-lift problems, overset meshing is not required, and work is underway to extend the off-body DG solver to body fitted meshes with dynamic AMR for hybrid RANS-LES as well as wall modeled LES applications.

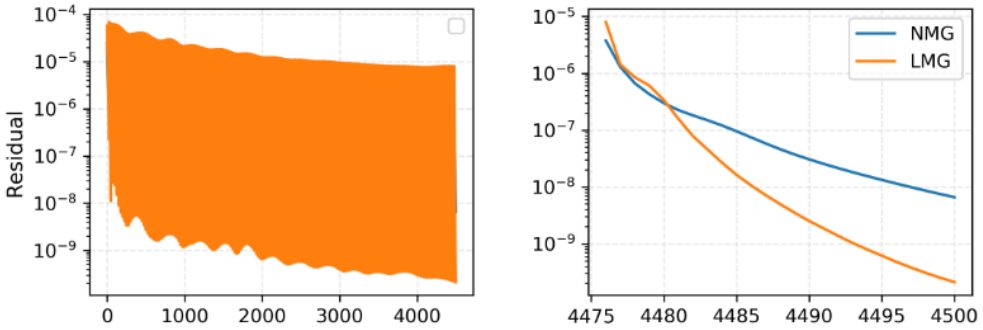

Figure 24. Iterative convergence for the BDF2 time-stepping scheme using 4-level linear (LMG) and nonlinear (NMG) multigrid employed by the near-body solver in the Hybrid RANS-LES simulations; (left) Convergence of linear multigrid over multiple time steps; (right) Comparison of linear and nonlinear multigrid over a single time step.

VI. Acknowledgements

We are grateful for computational time provided by the Advanced Research Computing Center at the University of Wyoming and the NCAR-Wyoming Supercomputer alliance.

References

[1]Long, M. and Mavriplis, D., "NSU3D Results for the First AIAA High-Lift Prediction Workshop," *AIAA Paper 2011-0863, 49th AIAA Aerospace Sciences Meeting, January 2011*.

[2]Mavriplis, D., Long, M., Lake, T., and Langlois, M., "NSU3D Results for the Second AIAA High-Lift Prediction Workshop," *Journal of Aircraft*, Vol. 52, No. 4, 2015, https://doi.org/10.2514/1.C033042.

[3]Mavriplis, D., Yang, Z., and Long, M., "Results using NSU3D for the first aeroelastic prediction workshop," *51st AIAA Aerospace Sciences Meeting, Grapevine TX, January 2013*, AIAA-Paper 2013-0786.

[4]Park, M., Laflin, K. R., Chaffin, M., Powell, N., and Levy, D. W., "CFL3D, FUN3D and NSU3D contributions to the fifth drag prediction workshop," Jan. 2013, AIAA Paper 2013-0050, 51st AIAA Aerospace Sciences Meeting, Grapevine TX.

[5]Sitaraman, J., Potsdam, M., Wissink, A., Jayaraman, B., Datta, A., Mavriplis, D., and Saberi, H., "Rotor loads prediction using helios: A multisolver framework for rotorcraft aeromechanics analysis," *Journal of Aircraft*, Vol. 50, No. 2, 2013, pp. 478–492.

[6]Allmaras, S. R., Johnson, F. T., and Spalart, P. R., "Modifications and Clarifications for the Implementation of the Spalart-Allmaras Turbulence Model," 2012, ICCFD7-1902, 7th International Conference on Computational Fluid Dynamics, Big Island, Hawaii, 9-13 July.

[7]Mavriplis, D. J. and Venkatakrishnan, V., "A unified multigrid solver for the Navier-Stokes equations on mixed element meshes," *International Journal of Computational Fluid Dynamics*, , No. 8, 1997, pp. 247–263.

[8]Mavriplis, D. J., Long, M., Lake, T., and Langlois, M., "NSU3D Results for the Second AIAA High-Lift Prediction Workshop," 2014, AIAA Paper 2014-748 52nd Aerospace Sciences Meeting, National Harbor, MD.

[9]Brazell, M. J., Kirby, A. C., Sitaraman, J., and Mavriplis, D. J., "A multi-solver overset mesh Approach for 3D mixed element variable order discretizations," AIAA Paper 2016-2053, 54th AIAA Aerospace Sciences Meeting, San Diego, CA., June 2016.

[10]Brazell, M. J., Kirby, A. C., and Mavriplis, D. J., "A high-order discontinuous-Galerkin octree-based AMR solver for overset simulations," AIAA Paper 2017-3944, 23rd AIAA Computational Fluid Dynamics Conference, Denver, CO., June 2017.

[11]Kirby, A. C., *Enabling high-order methods for extreme-scale simulations*, PhD Thesis, University of Wyoming, 2018.

[12]Brazell, M. J., Brazell, M. J., Stoellinger, M. K., Mavriplis, D. J., and Kirby, A. C., "Using LES in a Discontinuous Galerkin method with constant and dynamic SGS models," AIAA Paper 2015-0060, 53rd AIAA Aerospace Sciences Meeting, Kissimmee, FL., January 2015.

[13]Kirby, A. C., Mavriplis, D. J., and Wissink, A. M., "An Adaptive Explicit 3D Discontinuous Galerkin Solver for Unsteady Problems," AIAA Paper 2015-3046, 22nd AIAA Computational Fluid Dynamics Conference, Dallas, TX, June 2015.

[14]Burstedde, C., Wilcox, L. C., and Ghattas, O., "p4est: Scalable algorithms for parallel adaptive mesh refinement on forests of octrees," *SIAM Journal on Scientific Computing*, Vol. 33, No. 3, 2011, pp. 1103–1133.

[15]Smagorinsky, J., "General circulation experiments with the primitive equations: I. The basic experiment," *Monthly weather review*, Vol. 91, No. 3, 1963, pp. 99–164.

[16]Gassner, G. J., Winters, A. R., and Kopriva, D. A., "Split form nodal discontinuous Galerkin schemes with summation-by-parts property for the compressible Euler equations," *Journal of Computational Physics*, Vol. 327, 2016, pp. 39–66.

[17]Kirby, A. C. and Mavriplis, D. J., "Gpu-accelerated discontinuous galerkin methods: 30x speedup on 345 billion unknowns," *2020 IEEE High Performance Extreme Computing Conference (HPEC)*, IEEE, 2020, pp. 1–7.

[18]Brazell, M. J., Sitaraman, J., and Mavriplis, D. J., "An overset mesh approach for 3D mixed element high-order discretizations," *Journal of Computational Physics*, Vol. 322, 2016, pp. 33–51.

[19]Kirby, A. C., Brazell, M. J., Yang, Z., Roy, R., Ahrabi, B. R., Stoellinger, M. K., Sitaraman, J., and Mavriplis, D. J., "Wind farm simulations using an overset hp-adaptive approach with blade-resolved turbine models," *The International Journal of High Performance Computing Applications*, Vol. 33, No. 5, 2019, pp. 897–923.

[20]Edmonds, A. P., Hassanzadeh, A., Kirby, A. C., Mavriplis, D. J., and Naughton, J. W., "Effects of Blade Load Distributions on Wind Turbine Wake Evolution Using Blade-Resolved Computational Fluid Dynamics Simulations," AIAA Paper 2019-2081, 57th AIAA Aerospace Sciences Meeting, San Diego, CA., January 2019.

[21]Kirby, A. C., Hassanzadeh, A., Mavriplis, D. J., and Naughton, J. W., "Wind turbine wake dynamics analysis using a high-fidelity simulation framework with blade-resolved turbine models," AIAA Paper 2018-0256, AIAA SciTech Wind Energy Symposium, Kissimmee, FL., January 2018.

[22]Kara, K., Kirby, A. C., and Mavriplis, D. J., "Hover predictions using a high-order discontinuous galerkin off-body discretization," AIAA Paper 2020-0771, AIAA Scitech 2020 Forum, Orlando, FL., January 2020.

[23]Yang, Z., Kirby, A. C., and Mavriplis, D. J., "Comparison of Propeller-Wing Interaction Simulation using Different Levels of Fidelity," AIAA Paper 2022-1678, AIAA SCITECH 2022 Forum, San Diego, CA., January 2022.

[24]Mavriplis, D. J. and Mani, K., "Unstructured Mesh Solution Techniques using the NSU3D Solver," Jan. 2014, AIAA Paper 2014-081, 52nd Aerospace Sciences Meeting, National Harbor, MD.

[25]Mavriplis, D. J., "Progress in Computational Fluid Dynamics Discretizations Algorithms and Solvers for Aerodynamic Flows," *AIAA Journal*, Vol. 59, No. 12, 2021, pp. 5374–5397.